Neogene cratonic erosion fluxes and landform evolution processes from regional regolith mapping (Burkina Faso, West Africa)

Jean-Louis Grimaud, Dominique Chardon, Václav Metelka, Anicet Beauvais, Ousmane Bamba

▶ **To cite this version:**

Jean-Louis Grimaud, Dominique Chardon, Václav Metelka, Anicet Beauvais, Ousmane Bamba. Neogene cratonic erosion fluxes and landform evolution processes from regional regolith mapping (Burkina Faso, West Africa). Geomorphology, 2015, 241, pp.315 - 330. 10.1016/j.geomorph.2015.04.006 . ird-01419942

HAL Id: ird-01419942
https://ird.hal.science/ird-01419942

Submitted on 20 Dec 2016

HAL is a multi-disciplinary open access archive for the deposit and dissemination of scientific research documents, whether they are published or not. The documents may come from teaching and research institutions in France or abroad, or from public or private research centers.

L'archive ouverte pluridisciplinaire **HAL**, est destinée au dépôt et à la diffusion de documents scientifiques de niveau recherche, publiés ou non, émanant des établissements d'enseignement et de recherche français ou étrangers, des laboratoires publics ou privés.

*Revised manuscript with no changes marked
Click here to view linked References

Neogene cratonic erosion fluxes and landform evolution processes from regional regolith mapping (Burkina Faso, West Africa)

Jean-Louis Grimaud[1,2,3,4*], Dominique Chardon[1,2,3], Václav Metelka[1,2,3,5], Anicet Beauvais[6], Ousmane Bamba[7]

[1] Université de Toulouse, UPS (OMP), GET, 14 avenue Edouard Belin, 31400 Toulouse, France

[2] CNRS, GET, 31400 Toulouse, France

[3] IRD, UR 234, GET, 31400 Toulouse, France

[4] Now at St Antony Falls Laboratory, University of Minnesota, 2 Third Avenue SE, Minneapolis, MN 55414, USA

[5] Now at Center for Exploration Targeting, School of Earth and Environment, The University of Western Australia, (M006) 35 Stirling Highway, Crawley, WA 6009, Australia

[6] Aix Marseille Université, IRD, CNRS, CEREGE UM34, BP 80, 13545 Aix en Provence, Cedex 4, France

[7] Université de Ouagadougou, Laboratoire des géoressources et de l'Environnement, B.P. 7021, Ouagadougou, Burkina Faso

*** Corresponding author: jgrimaud@umn.edu**

Submitted to **Geomorphology,** 7 November 2014 (MS #5234)

Revised manuscript, submitted 1 April 2015

Abstract

The regionally correlated and dated regolith-paleolandform sequence of Sub-Saharan West Africa offers a unique opportunity to constrain continental-scale regolith dynamics as the key part of the sediment routing system. In this study, a regolith mapping protocol is developed and applied at the scale of Southwestern Burkina Faso. Mapping combines field survey and remote sensing data to reconstruct the topography of the last pediplain that formed over West Africa in the Early and Mid-Miocene (24-11 Ma). The nature and preservation pattern of the pediplain are controlled by the spatial variation of bedrock lithology and are partitioned among large drainage basins. Quantification of pediplain dissection and drainage growth allows definition of a cratonic background denudation rate of 2 m/My and a minimum characteristic timescale of 20 Ma for shield resurfacing. These results may be used to simulate minimum export fluxes of drainage basins of constrained size over geological timescales. Background cratonic denudation results in a clastic export flux of ~ 4 t/km^2/yr, which is limited by low denudation efficiency of slope processes and correlatively high regolith storage capacity of tropical shields. These salient characteristics of shields' surface dynamics would tend to smooth the reverine export fluxes of shields through geological times.

Keywords: Regolith; Pediment; Landform evolution processes; Sediment routing system; Source to sink.

1. Introduction

Interactions between landform evolution and regolith production and mobility over shields exert first-order controls on the source, pathways and fluxes of sediments

and solutes over very large emerged surfaces on geological timescales (e.g., Fairbridge and Finkl, 1980; Millot, 1983). Constraining these interactions on continental scales is therefore relevant to quantifying the contribution of shields, as opposed to that of orogens, to global sediment budgets and biogeochemical cycles in the context of long-term Cenozoic climate cooling (Ollier and Pain, 1996a; Molnar, 2004; Willenbring and von Blanckenburg, 2010; Goudie and Viles, 2012; Willenbring et al., 2013; Larsen et al., 2014). Large-scale studies of regolith transfers are also necessary for "source to sink" analyses of coupled drainage areas and sedimentary basins. The present contribution aims to quantify long-term landform evolution, regolith mobility and erosional export fluxes over a large region representative of shields' sediment routing systems.

Tropical shields are mantled by lateritic regoliths derived from intense rock weathering. Such lateritic covers are subject to remobilization by slope and fluvial processes, and the reworked regoliths are commonly re-weathered after transport (Ollier and Pain, 1996b). Renewed periods of regolith production by weathering and remobilization by pedimentation lead to the formation of composite landscapes consisting in a mosaic of lateritic paleo-landsurface remnants of various generations. Such landscapes are spectacularly preserved throughout Sub-Saharan West Africa, a region of more than 4.5 million km^2 over which a long-recognized Cenozoic regolith-paleo-landsurface sequence has been dated (Beauvais et al., 2008) and correlated (Beauvais and Chardon, 2013).

Here we develop a field- and remote sensing-based regolith-landform mapping protocol applied over Southwestern Burkina Faso (Fig. 1). The investigated area is large (ca. 300 x 300 km) and exposes the most widespread, type geologic and morphoclimatic configuration of the West African surface (granite-greenstone terrains and flat sandstones in the Guinean and Soudanian climatic zones i.e., between 10 and 13°N; Fig.

1). Given the constrained chronological framework of regolith-landform production over the sub-region, the selected area is therefore suitable for the characterization of landscape and regolith dynamics and the quantification of long-term (10^6-10^7 yr) erosion representative of shields surfaces. Regoliths are studied here both as in-situ produced or transported sediments and as paleo-landscape remnants. The obtained regolith-landform map allows evaluation of the nature, distribution and preservation of regolith mantles derived from a pediplain elaborated during the Early and Middle Miocene (ca. 24-11 Ma) over the sub-region. Based on this map, a topographic reconstruction of the pediplain is used to visualize regolith redistribution on slopes during pedimentation and to evaluate landscape and drainage evolution after its abandonment 11 Ma ago. Quantification of post-11 Ma dissection of the pediplain leads to estimation of a type-erosion flux for shields, emphasizing the low capacity of slope and alluvial processes to remove and export regolith mantles.

2. Geomorphological and geological background

2. 1. The West African geomorphic sequence and its regoliths

The following summary of the West African sequence of stepped lateritic paleo-landsurfaces (Fig. 2a) is based mostly on the works of Michel (1959, 1973, 1974), Eschenbrenner and Grandin (1970), Boulangé et al. (1973), Grandin (1976), Boulangé and Millot (1988) (see Chardon et al., 2006; Beauvais and Chardon, 2013).

Each member in the sequence has a distinct regolith cover and geomorphic character. The first two members of the sequence are the bauxitic and so-called Intermediate surfaces, which bear thick *in-situ* formed regoliths capped by bauxites and ferricretes, respectively. Bauxites are the end-product of a period of enhanced chemical weathering that started in the Late Cretaceous and culminated in the Mid-Eocene.

Bauxites seal a topography called the African Surface, which makes the present-day envelope of the West African relief. The Intermediate surface corresponds to a differentiated landscape carved in the African bauxitic surface. The following three stepped paleo-landsurfaces of the sequence are glacis (French term for pediments) called the High, Middle and Low glacis. Glacis surfaces are commonly covered by a detrital layer issued from degradation of earlier landforms. Each glacis has undergone weathering after pedimentation, indicating repeated transitions from arid or semi-arid pedimentation to seasonally contrasted or wet tropical weathering. Weathering periods generally ended with the formation of a ferricrete cementing the glacis surfaces and their detrital cover. Today, glacis occupy an overwhelming part of the West African landsurface (Beauvais and Chardon, 2013; Grimaud, 2014). The sequence is best preserved in the Sahelian and Soudanian climatic zones. The glacis, having undergone relief inversion, show evidence of degradation further south under the humid climate of the forest zone (Grandin, 1976). Though originally defined in the French-speaking countries, the sequence or elements of the sequence have been formally or implicitly identified and mapped in other countries of the sub-region (e.g., Fölster, 1969; Grandin and Hayward, 1975; Bowden, 1987; Durotoye, 1989; Thomas, 1980, 1994; Teeuw, 2002; see Beauvais and Chardon, 2013; Grimaud, 2014).

The Lower to Mid-Eocene age of peak weathering and abandonment of the bauxitic surface had long been stratigraphically bracketed (e.g., Millot, 1970). In absence of any stratigraphic constraints or radiometric data, the three glacis were thought to reflect Quaternary glacial – interglacial climatic cycles having led to the dissection of the Intermediate landscape of supposedly Latest Pliocene age (Michel, 1959). Absolute age constraints on the paleo-landsurface sequence were provided by radiometric ^{39}Ar-^{40}Ar dating of supergene cryptomelane ($K_{1-2}Mn_8O_{16}$, nH_2O) around

Tambao in Northeastern Burkina Faso (Hénocque et al., 1998; Colin et al., 2005; Beauvais et al., 2008; summarized in Beauvais and Chardon, 2013; Fig. 1). Data retrieved from the weathering profiles of each surface relict define five Ar-Ar age groups (ca. 59 - 45, 29 - 24, 18 -11, 7-6, and 3 Ma; Fig. 2b) bracketing periods of chemical weathering of the paleosurfaces. The lower limit of these age groups corresponds to the abandonment age of each paleosurface, i.e., the stabilization of the weathering front by the end of the weathering period preceding duricrusting and subsequent incision of each paleosurface (Fig. 2b). Abandonment ages are ca. 45 Ma for the African bauxitic surface and 24 Ma for the Intermediate surface. The High glacis surface developed between ca. 24 and 11 Ma with a predominance of weathering between 18 and 11 Ma. In Syama (Southern Mali; Fig. 1), Ar-Ar ages on supergene alunite and jarosite (Vasconcelos et al., 1994) confirm predominance of weathering conditions during elaboration of the Intermediate surface until the end of the Oligocene and weathering of the High glacis during the Mid-Miocene (Fig. 2b). Weathering and later abandonment of the Middle and Low glacis have occurred around 7-6 and 3 Ma, respectively (Fig. 2).

2. 2. Geological context

The study area belongs to the Paleoproterozoic portion of the West African craton exposed South of the Sahara (e.g., Feybesse et al., 2006; Fig. 1). This area comprises Birimian (2.2-2.1 Ga) granite-greenstone terrains over two-thirds of its surface and the Neoproterozoic sandstones of the Taoudeni basin, which were intruded by dolerite sills (Fig. 3). The basement comprises the Banfora, Houndé and Boromo greenstone belts and intervening granitoids (Baratoux et al., 2011; Metelka et al., 2011; Fig. 3b). Greenstones consist mainly of mafic volcanics (basalts and andesites) and

156 volcanosediments, whereas granitoids comprise TTG (tonalite - trondhjemite –
157 granodiorite) and granitic plutons. The escarpment delimiting the Banfora plateau marks
158 the southeastern boundary of the Taoudeni basin (Fig. 3a). The southern part of the
159 plateau bears the highest summits of the region and the height of the escarpment
160 decreases towards the NE. The study area mostly belongs to the Mouhoun drainage
161 system (the main stream of the Volta drainage system, i.e., the Black Volta) and is
162 fringed by the catchments of the Upper Niger River to the west, the Comoé River to the
163 southwest and the Nazinon River to the east (part of the Nakambé drainage system i.e.,
164 the White Volta; Figs. 1, 3).
165
166 2. 3. Earlier works on the study area
167 The pioneering study of Daveau et al. (1962) around Houndé and Gaoua (Fig. 3)
168 led to the identification of stepped lateritic landsurfaces and to the description of what
169 will be recognized later as the High glacis. Later on, the southern part of the study area
170 and its extension in the Ivory Coast became one of the first regions where the entire
171 West African regolith-landform sequence was thoroughly documented (Eschenbrenner
172 and Grandin, 1970). Boeglin and Mazaltarim (1989) and Boeglin (1990) later focused
173 on an area of ca. 50 x 30 km around Gaoua (Fig. 3), where they mapped the High glacis
174 relicts and performed a detailed geochemical study of their ferricretes. More recently,
175 Bamba (1996) and Bamba et al. (2002) have refined detailed mapping of the three glacis
176 around the Poura mine (left bank of the Mouhoun River, West of Tô; Fig. 3) to study
177 surface remobilization of gold. Lately, Butt and Bristow (2013), reporting on gold
178 prospects of the area, argued for the stepped character of the glacis and the detrital
179 nature of their ferricretes, which had been documented by geomorphologists since the
180 late 1950's (e.g., Michel, 1959; Daveau et al., 1962) but largely ignored since then.

3. Field relationships and regional-scale regolith-landform mapping

3. 1. Rationale

As opposed to the other regolith-landform associations of the lateritic paleo-landsurfaces sequence, High glacis remnants have both distinctive field and remotely-sensed mappable properties at the resolution of the digital data and given the size of the map area (see below). Our work therefore focused on the High glacis regolith-landform associations, which were characterized and mapped for evaluation of the pedimentation and weathering processes controlling the development of the High glacis paleo-landsurface. The topography of this paleo-landsurface was then reconstructed as a datum for the quantification of regional erosion after its abandonment. Higher paleo-landsurface relicts of the sequence (i.e., bauxitic and Intermediate) were already inherited landforms incorporated to the High glacis landscape and are still preserved in the current landscape. As seen below, their duricrusts are also found as reworked elements in the High glacis regoliths. Field characteristics of the higher landsurfaces are therefore described and their occurrences reported in the regolith-landform map. Relicts of the Middle and Low glacis (i.e., lower landsurfaces) occupy lower parts of today's landscape that have been excavated in the High glacis surface. Their field characteristics are briefly described below.

3. 2. Field typology of landforms and associated regoliths

3. 2. 1. Field survey

Our field observations were carried out at stations (Fig. 3b), which consist of areas of several km^2, where landscape analysis was undertaken by interpreting sceneries using 1/50 000 and 1/200 000 scale topographic maps. Mapping of regolith-landform

206 units was undertaken at key stations. Landscape interpretations/chronologies and
207 identification of paleo-landsurface relicts were complemented by in-situ examination of
208 the regolith along tracks through the landscape and at road cuts. This work included the
209 identification of the textures of the exposed lateritic weathering profile horizons and the
210 description of the sedimentary facies of the transported regoliths.
211
212 3. 2. 2. Higher landsurfaces
213 Bauxite relicts form mesas on the highest summits. On the basement, those
214 mesas are restricted to mafic substrates and their size is generally limited (i.e., less than
215 100 m wide) (Fig. 4a). In the Taoudeni basin, bauxitic plateaus are larger and mostly
216 restricted to dolerites (Figs. 4b, 4c). The bauxites have typical pink-whitish pisolithic
217 textures (Fig. 4d) or less evolved, nodular-mottled textures (Fig. 4e). In the Taoudeni
218 basin, particularly on dolerites, the Intermediate ferricrete caps gently dipping convex-
219 concave surfaces forming the downslope extension of the bauxitic plateaus (Figs. 4b,
220 4c). These ferricretes (Figs. 4f, 4g) show gradational variation in composition and
221 texture with the bauxites. This is interpreted to result from iron leaching that leads to
222 relative aluminum enrichment of the bauxites and net concomitant iron accumulation in
223 the ferricretes (Boulangé, 1986). Intermediate ferricretes on sandstones display typical
224 nodular textures (Fig. 4g). On the basement, the Intermediate ferricrete is rarely found
225 in-situ but rather as pebbles or cobbles reworked in the High glacis ferricrete (see
226 below). Instead, a residual "Intermediate relief" surrounds bauxitic duricrusts and may
227 be locally paved with a cemented scree of bauxite cobbles (Fig. 4a). Bauxites are
228 underlain by weathering profiles that are at least 80 m thick, as estimated on the
229 stripped slopes of mesas, whereas Intermediate weathering profiles exceed 20 m in
230 thickness.

231

232 3. 2. 3. High glacis

233 The best visible High glacis relicts are kilometer-scale plateaus (the largest ones
234 being concave) shallowly dipping away from the topographic massifs made of mafic
235 volcanics, which may carry higher relict paleo-landsurfaces (Fig. 5a). Such High glacis
236 relicts are often separated from the massifs by a peripheral hollow due to incision of
237 their upslope parts (see also Beauvais et al., 1999). This configuration indicates that the
238 High glacis has occupied large piedmonts that have been dissected. Dissection of the
239 High glacis ferricrete has carved 1 to 20 m-high scarps dominating slopes cut into soft
240 regoliths and covered by ferricrete debris (Figs. 5, 6a, 6b).

241 Most High glacis plateau ferricretes consist of a conglomerate ranging from
242 gravel to cobble, with a predominance of gravels mostly made of ferruginous nodules
243 (Fig. 6). Matrix silts and sands may bear quartz, particularly on volcano-sediments and
244 granitoids. Coarse gravels and cobbles are made of Intermediate-type ferricretes, vein
245 quartz and bauxites (Figs. 6a-6e). Conglomerates are commonly matrix- or block-
246 supported, suggesting emplacement by mudflow or debris flow process. Channels are
247 observed at the base of the ferricrete and decimeter- to meter-scale oblique
248 stratifications are recognized in the downslope parts of some large High glacis relicts
249 (Fig. 6d). The coexistence of mud or debris flow and alluvial facies in the High glacis
250 cover is indicative of interplay of slope and fluvial processes during pedimentation
251 (Dohrenwend and Parsons, 2009).

252 The noticeable absence of a mottled horizon under the glacis conglomerate or
253 exposure of deep portions of weathering profiles right under that cover (Figs. 6a, 6c)
254 indicates that these weathering profiles have been truncated before deposition of the
255 conglomerate. Duricrusting (i.e., iron impregnation or cementation) is mostly restricted

256 to the conglomerates cover (Figs. 6a, 6b). Still, soft ferricretes, i.e., pedogenic
257 impregnation of a mottled clay lateritic horizon (Tardy, 1997), are common under the
258 cemented conglomerates. This suggests renewed weathering along the upper fringe of
259 the truncated lateritic profiles under the conglomerates. At certain locations, the
260 ferricrete made of cemented debris flows may even be underlain by a type-succession of
261 weathering profile horizons (i.e., soft ferricrete, mottled layer, fine saprolite, coarse
262 saprolite; Figs. 6e, 6f), suggesting the full development of a weathering profile after
263 pedimentation.

264 On granitoids located away from topographic massifs (e.g., west of Djigoué and
265 south of Bobo Dioulasso, Tô region), the High glacis ferricretes are generally thinner
266 (0.5 - 2 m) and mantle smooth interfluves (Figs. 5c, 5d). Such ferricretes have
267 vermicular and nodular textures and are devoid of clasts. They appear less ferruginous
268 and less indurated than their plateau counterparts. These ferricretes show gradational
269 contacts with underlying soft ferricretes and are part of in-situ weathering profiles.
270
271 3. 2. 4. Lower landsurfaces
272 The restricted size of higher paleo-landsurfaces remnants is primarily due to the
273 development of the High glacis. But rejuvenation of the slopes of the residual reliefs
274 carrying those remnants and the formation of peripheral hollows (Fig. 5) is attributed to
275 the following periods of glacis formation. The landsurface between High glacis relicts
276 and the modern alluviums is almost exclusively occupied by the Middle and Low glacis.
277 These glacis may be stepped or may combine to form a single polygenic landsurface.
278 The regolith of the Middle and Low glacis is comparable to that of the High glacis, but
279 their ferricrete is generally thinner to absent and may be covered over large areas by
280 loose material made of reworked saprolite, sand and ferruginous gravels.

281

282 3. 3. Regional-scale regolith-landform mapping protocol

283 On basement terrains, High glacis units were manually mapped in GIS on the
284 basis of their airborne gamma ray spectrometry and their photo-interpretation signature
285 (Google Earth), both validated by the field survey / maps (Figs. 3, 7). Airborne gamma
286 ray spectrometry was acquired during the 1998–1999 SYSMIN (System for Mineral
287 Products) project (Metelka et al., 2011). Those data display uranium (U), potassium (K)
288 and thorium (Th) contents of the upper 30 cm of the Earth surface (Dickson and Scott,
289 1997). The spatial resolution of the data on the basement is 125 m (with an original line
290 spacing of 500 m). Spatial resolution of 250 m (line spacing of 1000 m) over the
291 Taoudeni basin has required resampling to 125 m in the area to obtain a harmonized
292 image. Both the raw and enhanced (Th/K ratio) gamma-ray spectrometry data where
293 used (Fig. 7) during the analysis and combined with the shaded relief maps of the
294 SRTM (Shuttle Radar Topographic Mission) data (90 m spatial resolution). The High
295 glacis ferricretes have a distinctive photo-interpretation texture that spatially matches
296 blue-green colors in raw gamma-ray data. This attests of a strong depletion in potassium,
297 and a relative enrichment in thorium and uranium as a result of weathering processes
298 (Dickson and Scott, 1997; Wilford et al., 1997; Metelka et al., 2011). However, uranium
299 has a complex behavior during weathering and regolith formation (Dickson and Scott,
300 1997; Wilford et al., 1997; Dequincey et al., 2002). Therefore, the Th/K ratio was
301 preferred to further enhance the signature of the High glacis ferricretes (in yellow-red)
302 and remove any regional gradients in the data (Figs. 7b, 7d).

303 The spatially homogeneous radiometric signature of the High glacis relicts
304 suggests that their ferricretes have been geochemically homogenized by weathering
305 despite the variability of their substrate. Indeed, trace element concentrations

306 systematically converge as a function of the Fe_2O_3 content of the ferricrete taken as an
307 index of their geochemical maturity (Boeglin and Mazaltarim, 1989; Boeglin, 1990).
308 Conversely, the ambiguous radiometric signature of the Middle and Low glacis may be
309 interpreted as a lower maturity of their ferricrete and a mixed signature of the material
310 covering their ferricrete.

311 The strong Th and exceptionally low K signatures of the Taoudeni basin (Figs.
312 7a, 7b) are explained by the mineralogy of the sandstones that are originally quartz rich
313 and correlatively poor in clays. The larger pixel size (250 m) of the gamma ray
314 spectrometry may have further modified the Th signature of High glacis ferricretes by
315 sampling other surface material with high Th content (e.g., Bauxite and Intermediate
316 duricrusts). Therefore, the high values (red colors) of Th/K ratio image (Fig. 7b) may
317 not only be due to High glacis ferricretes. Hence, regolith-landform mapping over the
318 Taoudeni basin was mainly based on photo-interpretation in Google Earth and field
319 observations.

320 Bauxite and Intermediate surface relict occurrences were mapped by photo-
321 interpretation, field observations and after Petit (1994). River plain sediments were
322 mapped mainly on the basis of their negligible relief and the characteristic geometries of
323 stream networks in the gamma-ray imagery. Because of the higher mobility of U
324 compared to Th, river plain sediments raw gamma-ray signature may indeed vary i.e.,
325 color of the source material (variable content of radioelements), very light to white color
326 (high U / Th / K signal), or very dark color (low U / Th / K signal). It might reflect the
327 composition of the source material, sediment mixing, or strong attenuation by
328 vegetation or water (Fig. 7a).

329

330 3. 4. Interpretation of the High glacis regolith-landform map

For the purpose of the interpretation, the mapped regolith-landform units were superimposed on the topography in Fig. 8 and on the geological map from Metelka et al. (2011) in Fig. 9. Comparison of these two maps highlights major contrasts in the pattern of High glacis relicts' distribution on either side of the main watersheds, even on the same geological substrate. This is particularly exemplified on TTG across the southwestern and eastern Mouhoun watersheds (Figs. 8, 9a). Density of High glacis relicts generally decreases when approaching the main streams (Fig. 8). Relicts are best preserved on TTG and granite (45 and 20% of the total surface of the relicts, respectively). Greenstones underlay less than 25% of the total area of the preserved High glacis ferricrete (Figs. 3b, 9c). Fifteen percent of the map area of the TTG and more than 20% of the granitoids are covered by High glacis ferricretes, whereas only 10% of the greenstones are covered (Fig. 9d).

Type-patterns of High glacis regolith-landforms may be distinguished in the study area (Figs. 5, 9, 10). In high relief volcanic terrains, High glacis relicts are well preserved on piedmonts (Fig. 10a), equally on greenstones and granitoids. Volcano-sedimentary-granitic terrains of moderate relief (e.g., Djigoué area) display High glacis relicts that once coated wide N-S trending valleys, which were in turn dissected by second-order narrower E-W oriented valleys (Fig. 10b). Over TTG terrains of the Comoé catchment (e.g., Dandougou-Bobodiolasso area), a very low relief and very low slope High glacis surface is preserved on sparse residual hills where the ferricrete may be dismembered into boulders resting on the soft ferricrete (Fig. 10c). The resulting landscape is a convexo-concave plain of low amplitude that is gently dipping towards the main stream (Fig. 10c). Equivalent TTG terrains in the Nakambe catchment reveal a better-preserved High glacis paleo-landsurface (see above), with planar to weakly concave relicts delineating a plain of very low-relief surface envelope (Fig. 10d).

356 The occurrence of strong and thick plateau ferricretes upon granitoids on the
357 piedmonts of volcanic reliefs contrasts with the weak and thin ferricretes preserved on
358 the same granitoids of the low land (Figs. 5a-5d). This reflects the high iron content and
359 thickness of the piedmont conglomerates made of reworked bauxitic and Intermediate
360 duricrusts that formed on iron-rich mafic rocks. On the contrary, low land ferricretes are
361 solely issued from in-situ weathering of iron poor granitoids. The limited lateritic cover
362 of mafic volcanics massifs further argues for the transfer of upland iron-rich duricrusts
363 as colluviums to the High glacis piedmonts. This transfer has resulted in net iron
364 accumulation on glacis surfaces further down in the landscape (Michel, 1973, 1974;
365 Beauvais et al., 1999).
366 The above analysis indicates that the High glacis landsurface was a pediplain,
367 defined as a surface of coalescent pediments (Maxson and Anderson, 1935). The spatial
368 distribution of these pediments and their regolith as well as the preservation pattern of
369 the High glacis pediplain are spatially controlled at various scales. A first, local control
370 of this distribution is exerted by the lithology of the bedrock. This sets the relief and
371 therefore the pedimentation process, as well as the weathering mode of the pediplain.
372 On a regional scale, pediplain dissection and erosion mode appear to have been
373 compartmentalized among drainage basins.
374
375 **4. Reconstruction of the Late Mid-Miocene pediplain and quantification of its**
376 **erosion**
377 4. 1. Methodology
378 The high density of High glacis relicts warrants reconstruction of the pediplain
379 they were part of. The reconstructed topography is a triangulated surface interpolated
380 from a set of geo-referenced points generated from the polygons of the High glacis

relicts using the DSI method (Gocad software; Mallet, 1992). Each High glacis polygon was converted to a grid of 500 m-spaced points inside its limits. The elevation of the SRTM digital elevation model, degraded to 500 m resolution, was then sampled for each point to form the High glacis relicts' elevation dataset. The interpolated surface was created from this dataset through a series of iterations. The number of surface's triangles, which reflected the distribution of the dataset for the first incremental surface, was increased at each iteration step, while the High glacis surface was forced to remain above the modern topography. This allowed for the inclusion of the reliefs dominating the pediplain and preserved the composite nature of the High glacis landscape. The resulting topography is shown on Fig. 11. Erosion post-dating the abandonment of the pediplain was obtained by subtracting the modern topography from that of the reconstructed pediplain (Figs. 11a-c). The drainage network and a slope map were then automatically extracted from both the modern and pediplain digital elevation models for comparison (Figs. 11d-h).

4. 2. Late Mid-Miocene topography and landscape dynamics

The pediplain displays the same first-order relief pattern as the current topography. The main divides such as the inselbergs and the main escarpment already existed at the time the pediplain was functional and did not migrate since then (Figs. 11a-b). The main river network was therefore already established since the Late Mid-Miocene with the exception of a few local river rearrangements (Figs. 11d, 11h). Our reconstruction does not allow for testing whether the Upper Mouhoun (flowing on the Taoudeni basin) was connected to the lower Mouhoun at the time of the High glacis (Fig. 11h). This rearrangement (Hubert, 1912; Palausi, 1959) occurred after the upper Mouhoun River, which used to flow northeastward into the Niger River since the

406 Eocene, formed the Gondo Plain internal delta (Beauvais and Chardon, 2013; Grimaud
407 et al., 2014; Fig. 1).
408 The spatial variability of the pediplain relief on the basement is representative of
409 the type-landscapes shown in Fig. 10 (comparisons with Figs. 9a, 12). One distinguishes
410 (i) an inselberg-studded pediplain around volcanic terrains, (ii) almost flat lands over
411 TTG, and (iii) a mix of the first two landscape types over volcano-sediments and
412 associated granite plutons. In the Taoudeni basin, the pediplain consists of wide and
413 shallowly dipping piedmonts connecting sandstone or higher landsurfaces plateaus to
414 the main streams.
415
416 4. 3. Interpretation of the pediplain dissection pattern
417 The pediplain has a low drainage density compared to that of the modern
418 landscape, with typical pediment widths of 10-20 km (up to 30 km over the sandstones;
419 Figs. 11, 12). Dissection of the High glacis landscape accompanied an increase in the
420 drainage density. The modern valley sides rarely exceed 5 km in width (Figs. 3, 8).
421 Dissection of the pediplain also resulted in an increase in slopes (Fig. 11g), which is in
422 agreement with the evolution from a pediplain towards narrower / deeper valleys. In
423 other words, the Middle and Low glacis, which contributed to the dissection of the
424 pediplain, never attained the width of the High glacis.
425 Post-11 Ma dissection of the pediplain is non-uniformly distributed, with
426 denudation depths ranging from 0 to 100 m and corresponding denudation from 0 to 10
427 m/my (Fig. 11c). Extreme denudations (> 60 m, > 5 m/My) over basement terrains are
428 concentrated on the steep slopes of residual reliefs (Figs. 6, 10, 11). Along the two main
429 streams, denudation is moderate to high (30 - 60 m; 2.5 - 5 m/My). The denudation is
430 rather uniformly distributed in the Comoé drainage, meanders being delineated by

denudation patterns in the vicinity of the Mouhoun River (Fig. 11c). The lowest erosion range (< 10 m, < 1 m/My) is recorded east of Tô, southeast of Bobo-Dioulasso and around Gaoua and Djigoué (Fig. 11c), in agreement with the high degree of preservation of the pediplain relicts (Fig. 8). The volume eroded from the pediplain over the map area represents a spatially averaged denudation of ca. 20 m, corresponding to a denudation rate of about 2 m/My.

Dissection of the Late Miocene pediplain affected the whole region and did not propagate upstream by scarp or knickzone retreat as advocated by King (1962) and as implicitly included in river profile inversion works based on stream power incision models (e.g., Paul et al., 2014). As an illustration, the bounding escarpment of the Taoudeni basin is stable since at least 11 Ma (Fig. 11) and most probably 45 Ma (see Grimaud et al., 2014). Higher erosion rates coincide with the main drains outside the High Mouhoun, suggesting a control of the stream power (e.g., Whipple and Tucker, 1999) on pediplain dissection. Moderate stream power in the rest of the river network would have preserved the pediplain from complete stripping. Scarps bounding High glacis relicts often coincide with second-order divides of the modern topography, indicating a component of slope retreat in the dissection of the pediplain. Meandering patterns of the Mouhoun River (Figs. 8, 11c) further suggest that channel migrations may have contributed to slope retreat. The typical retreat distance of the High glacis relicts' edges over the study area (1-10 km) suggests a retreat rate of 100-1000 m/My. Therefore, under the erosion dynamics at play since ca. 10 Ma and assuming an initial valley side width of 20 km (Fig. 12), a minimum of 20 My would be required to entirely resurface the High glacis pediplain.

5. Discussion

Our results complement denudation and incision rates estimated from differential elevation of sparse High glacis remnants and local base levels that have mean values of 5-7 m/My but non-uniform distributions over the sub region from 2 to 15 m/My (Beauvais and Chardon, 2013; Grimaud et al., 2014). This suggests a partitioning of erosion among geomorphic provinces, with implications on the spatial variability of the sediment routing system. This variability may be a function of the regional topographic relief and/or positive epeirogeny, which seem to focus higher denudation (Beauvais and Chardon, 2013; Grimaud et al., 2014). Importantly, this variability is also and primarily due to contrasted river network evolution among sub-drainage basins separated by stationary knickzones (Grimaud et al., 2014; this work).

Our approach has consisted in regional scale, volumetric quantification of denudation from a dated paleo-landscape datum, which enhances accuracy of denudation measurement over a West African province of lowest Neogene erosion. The obtained averaged denudation rate of 2 m/My is close to the lower limit of Cenozoic cratonic denudation rates measured worldwide (Beauvais and Chardon, 2013). Given the relevance of the size and morpho-geological context of the study area, we propose that this rate determines the background denudation 'noise' of shields. The Late Neogene increase in clastic sedimentation documented worldwide and particularly in African deltas such as that of the Niger (Séranne, 1999; Jermannaud et al., 2010; Fig. 1) should however be somehow included in the 2 m/My of background denudation averaged since the Early Late Miocene. This issue constitutes a sizable research challenge.

The material derived from dissection of the pediplain and removed since the Late Mid-Miocene was made of regolith, i.e. the High glacis cover and its underlying laterites. Indeed, no outcrop of significant surface / height has been exhumed since the

481 abandonment of the pediplain. The fact that only the main stream channels locally flow
482 atop the bedrock and that an averaged denudation of less than 20 m since abandonment
483 of the pediplain is estimated further argues for denudation being restricted to the
484 regolith. Denudation is however not strictly weathering-limited because if glacis
485 typically cut preexisting and potentially old regoliths (i.e., Late Cretaceous to Eocene
486 and Oligocene for the bauxitic and Intermediate weathering episodes, respectively,
487 Figure 2), they rarely attained the bedrock. Therefore, although weathering is
488 instrumental in producing regolith mantles available to future stripping (Fairbridge and
489 Finkl, 1980), low abrasion power of the pedimentation process combined with a
490 probably limited transport capacity of the river network should be regarded as the
491 limiting factor of tropical shields denudation.

492 The minimum characteristic timescale of 20 My for shield resurfacing indicated
493 by post-Mid-Miocene drainage growth reinforces the view that shields are non-
494 equilibrium landscapes, which increase their relief through geological time by
495 preserving old landforms (Thomas, 1989; Twidale, 1991; Bishop, 2007; Beauvais and
496 Chardon, 2013). A long resurfacing timescale also implies the high sediment retention
497 capacity of shields as those sediments stem from weathering mantles dating back from
498 at least the Early Paleogene and have been slowly recycled through the landscape since
499 then. This suggests that weathering and slope processes play a major role, comparable
500 to or greater than sediment transport by rivers (Métivier and Gaudemer, 1999;
501 Jerolmack and Paola, 2010) in “shredding” and particularly smoothing or buffering
502 climatic signals in the sedimentary record. Still, the ubiquitous character of the West
503 African lateritic paleo-landsurfaces sequence and its chronology would suggest that
504 Cenozoic landscape rejuvenation and sediment fluxes were punctuated by major
505 climatic periods. Subdued clastic exports are indeed expected for time intervals of

enhanced weathering during the Lower and Mid-Eocene, Late Oligocene, Mid Miocene, Latest Miocene and Latest Pliocene (e.g., Fig. 2b).

The background denudation rate of 2 m/My may be converted into a volumetric export rate of 2 x 10^{-3} $km^3/km^2/My$ and a clastic yield of 4 $t/km^2/yr$, considering an effective grain density of 2,500 kg/m^3 (estimated from a bulk density of 2,000 kg/m^3 and a 20 % porosity) for the stripped regolith. This value corresponds to the lower limit of modern West African solid river loads (3.5 - 300 $t/km^2/yr$) and to the 4 $t/km^2/yr$ measured at the outlet of the Volta catchment (Milliman and Farnsworth, 2013). Therefore, cratonic erosion fluxes derived from a 2 m/My denudation rate appear to be realistic for low-capacity shield drainage systems on geological timescale. Conversely, this could suggest that the lower limit of large tropical shields catchments yields is governed by a cratonic background denudation noise. Importantly, background cratonic denudation of 2 m/My may be used to simulate the minimum export fluxes of drainage basins of constrained size over geological timescales.

9. Conclusions

Regional regolith-landform mapping allows characterizing surface dynamics, weathering patterns, paleotopography and dissection mechanisms of the last pediplain formed over West Africa from Early to Mid-Miocene. The nature and preservation / dissection patterns of the pediplain are controlled by the spatial distribution of bedrock lithologies and are partitioned between large drainage basins. Quantification of the post Mid-Miocene dissection of the pediplain determines a cratonic background denudation noise of 2 m/My and a minimum shield resurfacing characteristic timescale of 20 My. The minimum clastic yield of the major African catchments seems to be currently dominated by such a cratonic noise. Our results, once combined with landscape /

weathering chronologies, point to the shields' high storage capacity of sediments, consisting exclusively of regoliths that have been mainly recycled in the landscapes since the Late Cretaceous. Such a slow regolith turnover is due to the low efficiency of slope denudation processes by pedimentation and would tend to smooth riverine export fluxes of shields over geological time scales.

Acknowledgments

This work was funded by WAXI, the CNRS and the ANR TopoAfrica (ANR-08-BLAN-572 0247-02). The manuscript benefited from the comments of R. Teeuw and an anonymous referee as well as from editorial suggestions by A. Plater. We thank M. Jessell, D. Rouby, L. Baratoux and D. Huyghe for discussions and support and A. Fofana for participation in the fieldwork. We acknowledge AMIRA International and the industry sponsors, including AusAid and the ARC Linkage Project LP110100667, for their support of the WAXI project (P934A) as well as the Geological Surveys / Departments of Mines in West Africa as sponsors in kind of WAXI.

547 **References**

548 Bamba, O., 1996. L'or disséminé dans les Albitites de Larafella (Burkina Faso),
549 évolution dans les altérites et les cuirasses ferrugineuses : Métallogénie -
550 Pétrologie – Géomorphologie. PhD Thesis, Aix-Marseille III University,
551 Marseille, France, 261 pp.
552 Bamba, O., Parisot, J.-C., Grandin, G., Beauvais, A., 2002. Ferricrete genesis and
553 supergene gold behaviour in Burkina Faso, West Africa. Geochem. Explor.
554 Environ. Anal. 2(1), 3-13.
555 Baratoux, L., Metelka, V., Naba, S., Jessell, M.W., Grégoire, M., Ganne, J., 2011.
556 Juvenile Paleoproterozoic crust evolution during the Eburnean orogeny (~2.2–
557 2.0 Ga), Western Burkina Faso. Precambrian Res. 191(1–2), 18-45.
558 Beauvais, A., Chardon, D., 2013. Modes, tempo and spatial variability of Cenozoic
559 cratonic denudation: The West African example. Geochem. Geophys. Geosyst.
560 14, 1590–1608.
561 Beauvais, A., Ruffet, G., Hénocque, O., Colin, F., 2008. Chemical and physical erosion
562 rhythms of the West African Cenozoic morphogenesis: The ^{39}Ar-^{40}Ar dating of
563 supergene K-Mn oxides. J. Geophys. Res. 113, F04007.
564 Beauvais, A., Ritz, M., Parisot, J.-C., Dukhan, M., Bantsimba, C., 1999. Analysis of
565 poorly stratified lateritic terrains overlying a granitic bedrock in West Africa,
566 using 2-D electrical resistivity tomography. Earth Planet. Sci. Lett. 173(4), 413-
567 424.
568 Bishop, P., 2007. Long-term landscape evolution: linking tectonics and surface
569 processes. Earth Surf. Proc. Land. 32(3), 329-365.

570 Boeglin, J.-L., 1990. Évolution minéralogique et géochimique des cuirasses
571 ferrugineuses de la région de Gaoua (Burkina Faso). PhD Thesis, Louis Pasteur
572 University, Strasbourg, 228 pp.
573 Boeglin, J.-L., Mazaltarim, D., 1989. Géochimie, degré d'évolution et lithodépendance
574 des cuirasses ferrugineuses de Gaoua au Burkina Faso. Sci. Géol. Bull. 42(1),
575 27-44.
576 Boulangé, B., 1986. Relation between lateritic bauxitization and evolution of landscape.
577 Trav. Int. Com. Stud. Bauxite, Alumina & Aluminum (ICSOBA) 16-17, 155-
578 162.
579 Boulangé, B., Millot, G., 1988. La distribution des bauxites sur le craton ouest-africain.
580 Sci. Géol. Bull. 41(1), 113-123.
581 Boulangé, B., Sigolo, J.B., Delvigne, J., 1973. Descriptions morphoscopiques,
582 géochimiques et minéralogiques des faciès cuirassés des principaux niveaux
583 géomorphologiques de Côte d'Ivoire. Cah. ORSTOM, sér. Géol. 5(1), 59-81.
584 Bowden, D.J, 1987. On the composition and fabric of the footslop laterites (duricrusts)
585 of the Sierra Leone, West Africa, and their geomorphological significance. Z.
586 Geomorphol., Suppl. 64, 39-53.
587 Butt, C.R.M., Bristow, A.P.J., 2013. Relief inversion in the geomorphological evolution
588 of sub-Saharan West Africa. Geomorphology 185, 16-26.
589 Dequincey, O., Chabaux, F., Clauer, N., Sigmarsson, O., Liewig, N., Leprun, J.C., 2002.
590 Chemical mobilizations in laterites: evidence from trace elements and 238U-
591 234U-230Th disequilibria, Geochim. Cosmochim. Acta, 66, 1197-1210.
592 Chardon, D., Chevillotte, V., Beauvais, A., Grandin, G., Boulangé, B., 2006. Planation,
593 bauxites and epeirogeny: one or two paleosurfaces on the West African
594 margin? Geomorphology 32, 273-282.

595 Colin, F., Beauvais, A., Ruffet, G., Hénocque, O., 2005. First $^{40}Ar/^{39}Ar$ geochronology
596 of lateritic manganiferous pisolites; implications for the Palaeogene history of a
597 West African landscape. Earth Planet. Sci. Lett. 238(1-2), 172-188.
598 Daveau, S., Lamotte, M., Rougerie, G., 1962. Cuirasses et chaînes birrimiennes en
599 Haute-Volta. Ann. Géogr. Fr. 387, 260-282.
600 Dickson, B.L., Scott, K.M., 1997. Interpretation of aerial gamma-ray surveys – adding
601 the geochemical factors. AGSO J. Aust. Geol. Geophys. 17(2), 187–200.
602 Dohrenwend, J.C., Parsons, A.J., 2009. Pediments in Arid Environments. In: Parsons,
603 A., Abrahams, A. (Eds.), Geomorphology of Desert Environments. Springer
604 Netherlands, The Netherlands, pp. 377-411.
605 Durotoye, B., 1989. Quaternary sediments in Nigeria. In Kogbe, C.A. (Ed), Geology of
606 Nigeria (second edition). Rock View International, Paris, pp. 431-444.
607 Eschenbrenner, R., Grandin G., 1970. La séquence de cuirasses et ses différenciations
608 entre Agnibiléfrou et Diébougou (Haute-Volta). Cah. ORSTOM, Sér. Géol.
609 2(2), 205-246.
610 Fairbridge, R.W., Finkl, C.W., 1980. Cratonic erosional unconformities and peneplains.
611 J. Geol. 88, 69-86.
612 Feybesse, J.-L., Billa, M., Guerrot, C., Duguey, E., Lescuyer, J.-L., Milesi, J.-P.,
613 Bouchot, V., 2006. The Paleoproterozoic Ghanaian province: Geodynamic
614 model and ore controls, including regional stress modeling. Precambrian Res.
615 149(3–4), 149-196.
616 Fölster, H., 1969. Late Quaternary erosion phases in SW Nigeria. Bull. Ass. Sénég. Et.
617 Quatern. Ouest afr. 21, 29-35.
618 Goudie, A.S., Viles, H.A., 2012. Weathering and the global carbon cycle:
619 geomorphological perspectives. Earth-Sci. Rev. 113(1-2), 59-71.

620 Grandin, G., Hayward, D.F., 1975. Aplanissements cuirassés de la péninsule de
621 Freetown (Sierra Leone). Cah. ORSTOM, sér. Géol. 7(1), 11-16.
622 Grandin, G., 1976. Aplanissements cuirassés et enrichissement des gisements de
623 manganèse dans quelques régions d'Afrique de l'Ouest. Mém. ORSTOM 82, 1-
624 276.
625 Grimaud, J.-L., 2014. Dynamique long-terme de l'érosion en contexte cratonique :
626 l'Afrique de l'Ouest depuis l'Eocène. PhD Thesis, Toulouse University,
627 Toulouse, France, 300 pp.
628 Grimaud, J.-L., Chardon, D., Beauvais, A., 2014. Very long-term incision dynamics of
629 big rivers. Earth Planet. Sci. Lett. 405, 74-84.
630 Hénocque, O., Ruffet, G., Colin, F., Féraud, G., 1998. 40Ar/39Ar dating of West
631 African lateritic cryptomelanes. Geochim. Cosmochim. Acta 62(16), 2739-
632 2756.
633 Hubert, H., 1912. Sur un important phénomène de capture dans l'Afrique occidentale.
634 Ann. Géog. Fr. 21 (117), 251-262.
635 Jermannaud, P., Rouby, D., Robin, C., Nalpas, T., Guillocheau, F., Raillard, S., 2010.
636 Plio-Pleistocene sequence stratigraphic architecture of the Eastern Niger Delta:
637 A record of eustasy and aridification of Africa. Mar. Pet. Geol. 27, 810-821.
638 Jerolmack, D.J., Paola, C., 2010. Shredding of environmental signals by sediment
639 transport. Geophys. Res. Lett. 37(19), L19401.
640 King, L.C., 1962. The Morphology of the Earth. Oliver and Boyd, Edinburgh, 799 pp.
641 Larsen, I.J., Montgomery, D.R., Greenberg, H.M., 2014. The contribution of mountains
642 to global denudation. Geology 42(6), 527–530.
643 Mallet, J.-L., 1992. Discrete smooth interpolation in geometric modelling. Computer-
644 Aided Design 24(4), 178-191.

645 Maxson, J.H., Anderson, G.H., 1935. Terminology of surface forms of the erosion cycle.
646 J. Geol. 43, 88-96.
647 Metelka, V., Baratoux, L., Naba, S., Jessell, M.W., 2011. A geophysically constrained
648 litho-structural analysis of the Eburnean greenstone belts and associated
649 granitoid domains, Burkina Faso, West Africa. Precambrian Res. 190(1–4), 48-
650 69.
651 Métivier, F., Gaudemer, Y., 1999. Stability of output fluxes of large rivers in South and
652 East Asia during the last 2 million years: implications on floodplain processes.
653 Basin Res. 11(4), 293-303.
654 Michel, P., 1959. L'évolution géomorphologique des bassins du Sénégal et de la Haute-
655 Gambie, ses rapports avec la prospection minière. Rev. Géomorph. Dyn. 10,
656 117-143.
657 Michel, P., 1973. Les bassins des fleuves Sénégal et Gambie : étude géomorphologique.
658 Mém. ORSTOM 63, 1-752.
659 Michel, P., 1974. Les glacis cuirassés d'Afrique occidentale et centrale. In:
660 Géomorphologie des glacis. Colloques scientifiques de l'Université de Tours,
661 Tours, France (1974), pp.70-80.
662 Milliman, J.D., Farnsworth, K.L., 2013. River Discharge to the Coastal Ocean: A
663 Global Synthesis. Cambridge University press, Cambridge, 392 pp.
664 Millot, G., 1970. Geology of clays. Springer Verlag, Berlin, 429 pp.
665 Millot, G., 1983. Planation of continents by intertropical weathering and pedogenetic
666 processes. In: Melfi, A.J., Carvalho, A. (Eds.), Lateritisation Processes.
667 Proceedings of the IInd international Seminar on Lateritisation Processes, Sao
668 Paulo, Brazil (1982), pp. 53–63.

669 Molnar, P., 2004. Late Cenozoic increase in accumulation rates of terrestrial sediment:
670 How Might Climate Change Have Affected Erosion Rates? Ann. Rev. Earth
671 Planet. Sci. 32(1), 67-89.
672 Ollier, C.D., Pain, C.F., 1996a. Regolith, soils and landforms. John Wiley & Sons,
673 Chichester, 316 pp.
674 Ollier, C.D., Pain, C.F., 1996b. Regolith stratigraphy: principles and problems. AGSO J.
675 Aust. Geol. Geophys. 16, 197-202.
676 Palausi, G., 1959. Contribution à l'étude géologique et hydrogéologique des formations
677 primaires au Soudan et en Haute-Volta. Bull. Serv. Géol. Prosp. Min. 33, 1 -
678 209.
679 Paul, J.D., Roberts, G.G., White, N., 2014. The African landscape through space and
680 time, Tectonics 33, 898-935.
681 Petit, M., 1994. Carte Géomorphologique du Burkina Faso au 1/1 000 000. ORSTOM -
682 University of Ouagadougou, Ouagadougou, Burkina Faso (unpublished).
683 Séranne, M., 1999. Early Oligocene stratigraphic turnover on the West Africa
684 continental margin: a signature of the Tertiary greenhouse-to-icehouse
685 transition? Terra Nova 11(4), 135-140.
686 Tardy, Y., 1997. Petrology of laterites and tropical soils. Balkema, Rotterdam, 408 pp.
687 Teeuw, R.M., 2002. Regolith and diamond deposits around Tortiya, Ivory Coast, West
688 Africa. *CATENA 49*(1-2), 111-127.

689 Thomas M.F., 1980. Timescales of landform development on tropical shields — a study
690 from Sierra Leone. In: Cullingford, R.A., Davidson, D.A., Lewin J. (Eds.),
691 Timescales in Geomorphology. Wiley, Chichester, pp. 333–354.

692 Thomas, M.F., 1989. The role of etch processes in landform development II. Etching
693 and the formation of relief. Z. Geomorphol. 33(3), 257-274.
694 Thomas, M.F., 1994. Geomorphology in the Tropics: A Study of Weathering and
695 Denudation in Low Latitudes. Wiley & Sons, New York, 482 pp.
696 Twidale, C.R, 1991. A model of landscape evolution involving increased and increasing
697 relief amplitude. Z. Geomorphol. 35(1), 85-109.
698 Vasconcelos, P.M., Brimhall, G.H., Becker, T.A., Renne, P.R., 1994. $^{40}Ar/^{39}Ar$ analysis
699 of supergene jarosite and alunite: Implications to the paleoweathering history
700 of the western USA and West Africa. Geochim. Cosmochim. Acta 58(1), 401-
701 420.
702 Whipple, K.X., Tucker, G.E., 1999. Dynamics of the stream-power river incision
703 model; implications for height limits of mountain ranges, landscape response
704 timescales, and research needs. J. Geophys. Res. 104(B8), 17.
705 Wilford, J.R., Bierwirth, P.N., Craig, M.A., 1997. Application of airborne gamma-ray
706 spectrometry in soil/regolith mapping and applied geomorphology. AGSO J.
707 Aust. Geol. Geophys. 17, 201-216.
708 Willenbring, J.K., von Blanckenburg, F., 2010. Long-term stability of global erosion
709 rates and weathering during late-Cenozoic cooling. Nature 465, 211-214.
710 Willenbring, J.K., Codilean, A.T., McElroy, B., 2013. Earth is (mostly) flat:
711 Apportionment of the flux of continental sediment over millennial time scales.
712 Geology 41, 343–346.
713

Figures Captions

Figure 1: Simplified geology of sub-Saharan West Africa. The study area is shown by a red frame (map modified from Feybesse et al., 2006).

Figure 2: (a) Lateritic paleo-landsurface sequence and incision chronology of West Africa (compiled after Michel, 1973; Beauvais et al., 2008; Beauvais and Chardon, 2013 and modified after Grimaud et al., 2014). (b) Synthesis of Ar-Ar age data obtained on supergene Mn oxides. Colored time slices represent the main periods of weathering correlated with the successive paleolandsurfaces, based on dating of cryptomelane in Tambao (after Beauvais et al., 2008; Beauvais and Chardon, 2013). Ages reported from Syama were obtained on alunite and jarosite (after Vasconcelos et al., 1994). Note that only alunite and jarosite ages with error of less than 5 Ma are reported. Terminology of the paleo-landsurfaces: Bx – Bauxite; Int – Intermediate; HG – High glacis; MG – Middle glacis; LG – Low glacis. Syama and Tambao are located on Fig. 1.

Figure 3: Topography and simplified geology of the study area (see Fig. 1 for location). Shaded topography (a) based on SRTM digital elevation model smoothed to 500 m resolution. Simplified geology (b) is adapted from Baratoux et al. (2011). Field stations are shown by yellow dots.

Figure 4: Illustrations of field characteristics of the higher lateritic paleo-landsurfaces in Southwestern Burkina Faso. (a) Bauxite-capped greenstone massif, 15 km SE of Iridiaka (location on Fig. 3; see also Fig. 9b). The bauxitic plateau is ca. 300 m long. (b) – (c) South-looking Google Earth view and interpretation of a dolerite topographic massif near Kokoro, Taoudeni basin (location on Figure 3; Vertical exaggeration x3).

740 HG - High glacis. (d) Close-packed pisolithic texture of the Iridiaka bauxite shown in
741 (a). (e) Nodular - mottled texture of the Kokoro bauxite shown in (b) and (c). (f)
742 Massive nodular facies of the Intermediate ferricrete shown in (b) - (c). (g) Iron
743 nodulation at the root of the Intermediate ferricrete over sandstones, Taoudeni basin
744 north of Banfora (location on Fig. 3).
745
746 **Figure 5:** Illustrations of the High glacis relict landforms. (a) - (b) Google Earth view
747 and interpretation of the eastern piedmont of a volcanic inselberg near Dano (Fig. 3). (c)
748 - (d) Google Earth view and interpretation of parse High glacis relict hills resulting from
749 dissection by a dendritic river network on granitic substrate, Dandougou area (Fig. 3).
750 High glacis relicts are shown in green. Dip symbols indicate High glacis
751 paleolandsurface direction and sense of slope. (e) Gently west-dipping plateau bounded
752 by a 10-15 m high scarp (5 km West of Gaoua, view looking SW). (f) Closer view of
753 the plateau edge shown in (e). (g) Scarp carved in >10 m thick ferricrete cementing
754 glacis cover material (in between Djigoué and Gaoua).
755
756 **Figure 6:** Illustrations of High glacis regoliths. (a) Base of a High glacis ferricrete
757 truncating a granitic weathering profile (Djigoué area). Light-colored cobbles in the
758 ferricrete are quartz clasts. (b) Details of a High glacis ferricrete showing cobbles of
759 Intermediate ferricrete and quartz in a finer grained conglomerate, base of the cliff
760 shown in Fig. 5g. (c) Cemented debris flow on dolerites near Kokoro (site of Fig. 4b,
761 4c). Light-colored debris consists of bauxite clasts. The flow rests upon a truncated
762 weathering profile developed from dolerites that remain as core stones in the saprolite.
763 (d) Alluvial channel at the base of High glacis ferricrete carved into weathered
764 sandstones of the Taoudeni basin (South of Bobo-Dioulasso). (e) Cobble of

765 Intermediate ferricrete cemented in a High glacis ferricrete. (f) Weathering profile
766 underlying that same ferricrete (northeast of Dédougou). See Fig. 3 for locations.
767
768 **Figure 7:** Ternary image of the airborne gamma-ray spectrometry survey (a) and the
769 enhanced Th/K ratio image of the survey (b) over the study area. (c) - (f) Details of the
770 datasets that were combined for the identification and mapping of High glacis relicts on
771 the example of the Djigoué area. (c) Airborne gamma-ray spectrometry 100-250 m
772 (resampled to 100 m) resolution ternary image. The area corresponding to the High
773 glacis ferricrete has a strong thorium signature in green and a medium uranium
774 signature in blue. In this area, the substrate has a strong potassium signature in red. (d)
775 Ratio image of thorium over potassium (100 m resampled resolution). The High glacis
776 ferricrete, enriched in thorium and depleted in potassium, is highlighted in white to red
777 colors. (e) 15-m resolution LANDSAT image. (f) Mapping by construction of the
778 polygons (crossed frame) corresponding to the High glacis ferricrete, superimposed on
779 the SRTM topography. Field stations are shown as yellow dots. Rivers are shown in
780 white.
781
782 **Figure 8:** Regolith-landform map superimposed on the STRM digital elevation model
783 (90 m resolution). Black boxes correspond to the frame of the maps shown in Fig. 10.
784
785 **Figure 9:** (a) Regolith-landform map superimposed on the geology that is simplified
786 from Metelka et al. (2011). (b) Synthetic regional cross-section of the study area. The
787 line of section is located in (a). Trace of the HG surface is shown in dark green (dashed
788 where eroded). (c) Histogram of the High glacis ferricrete total area partitioned on each
789 substrate. (d) Proportion of the High glacis surface on each lithology covered by

ferricrete. For the whole Birimian basement, this percentage is of about 11 %. Dolerites and sandstones were not distinguished in the Taoudeni basin.

Figure 10: Maps and cross-sections of type-landscapes on basement terrains. Frames of the maps are located on Fig. 8. Dip symbols represent the direction and sense of slope of the High glacis relicts (in green). Dashed lines on the maps are lithological boundaries (see Fig. 9a).

Figure 11: (a) Modern topography based on SRTM digital elevation model smoothed to 500 m resolution. (b) Reconstructed topography of the High glacis pediplain. (c) Denudation map obtained by subtracting present-day topography from that of the High glacis stage. (d) River network automatically extracted from the digital elevation model of the High glacis pediplain in Fig. 11b. Red arrows represent drainage rearrangements in between the High glacis stage (d) and the present-day landscape (a). (e) Slope map of the current topography derived from (a). (f) Slope map of the High glacis pediplain derived from (b). (g) Comparative slope distribution for the High glacis and modern topographies. (h) River network automatically extracted from the present-day topography in Fig. 11a.

Figure 12: Geomorphological map of the High glacis pediplain before its abandonment in the Earliest Late-Miocene (ca. 11 Ma). The thick black dashed line represents the boundary of the Mouhoun catchment.

Figure 1

Click here to download high resolution image

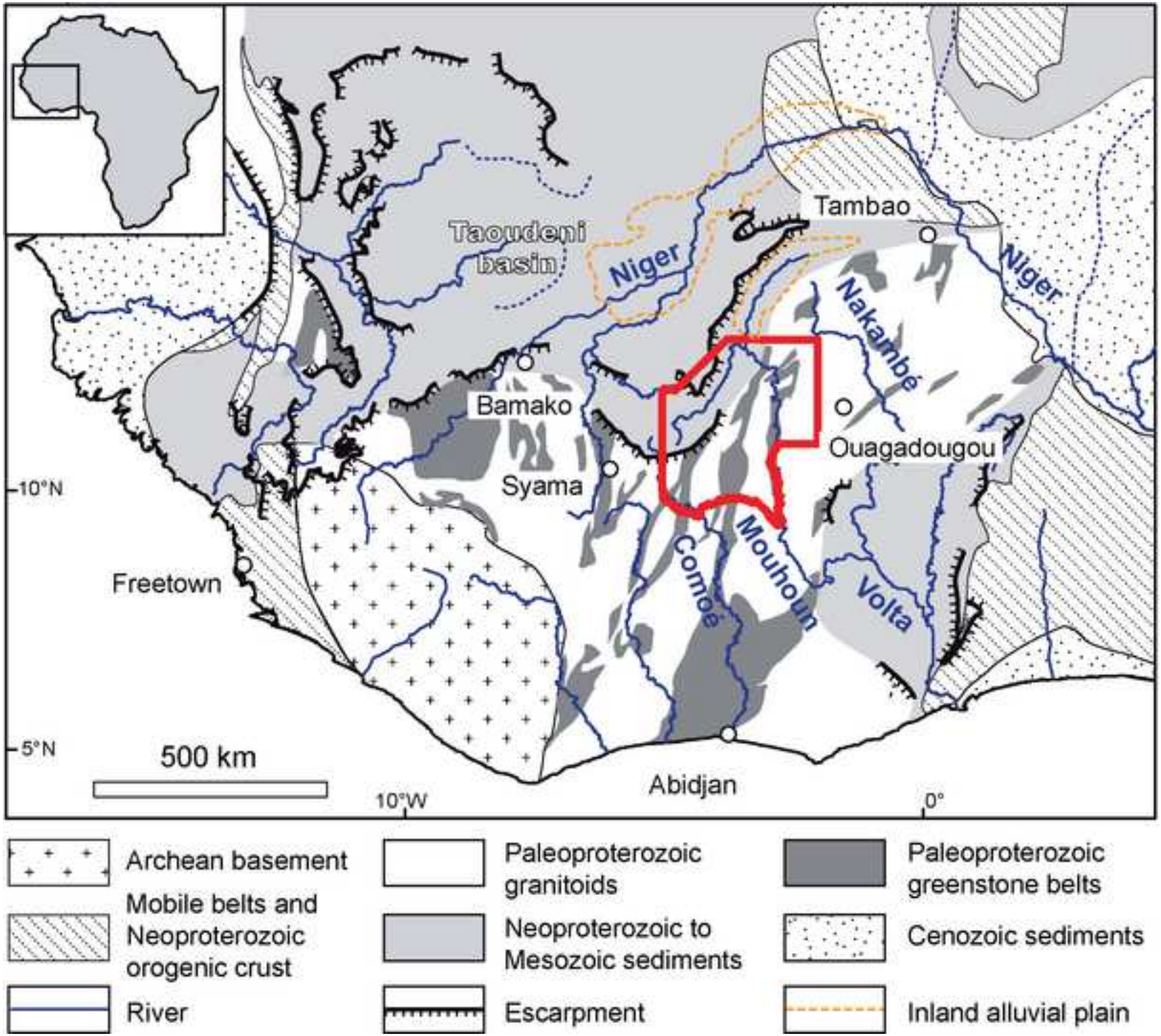

Figure 2

Click here to download high resolution image

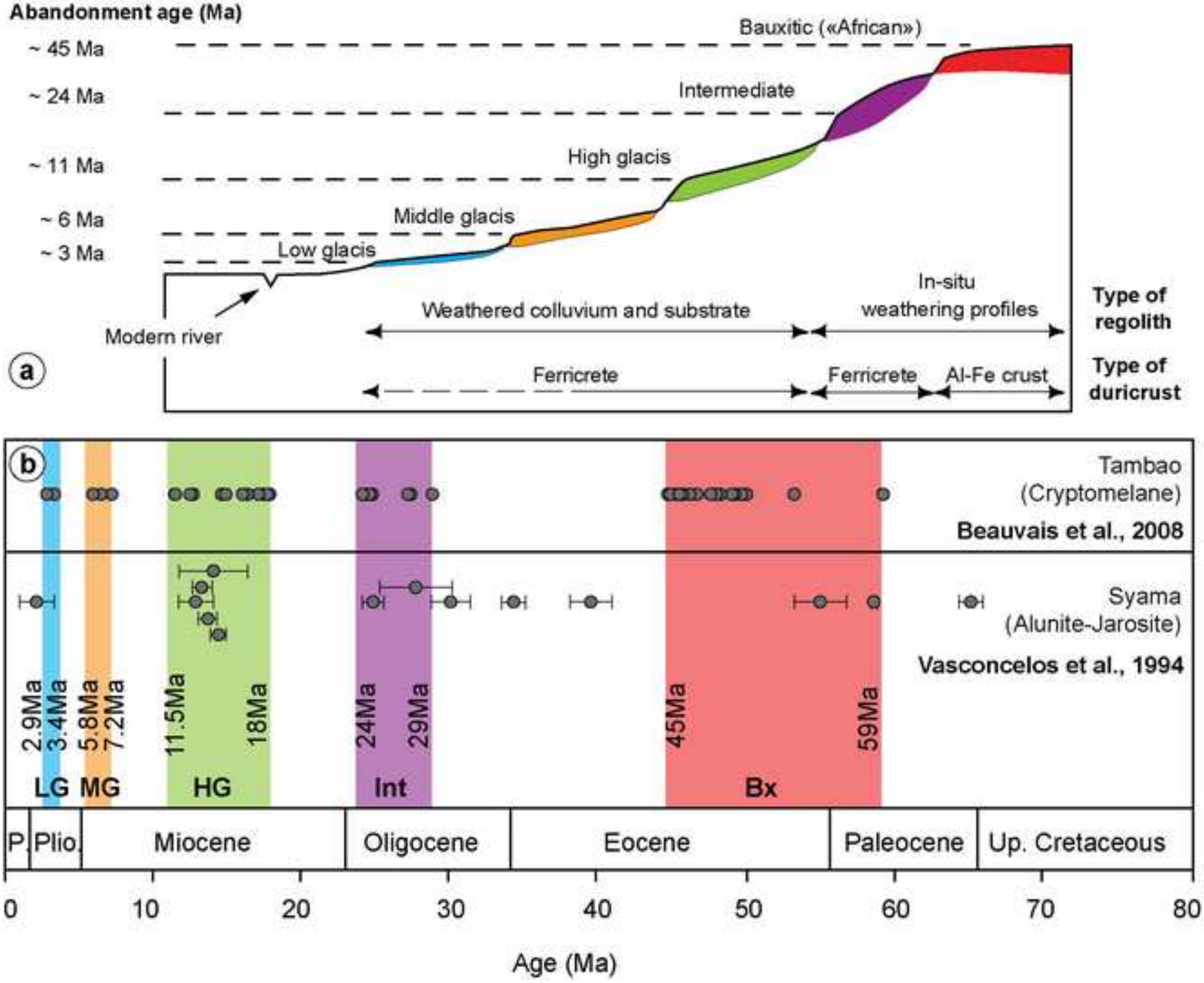

Figure 3

Click here to download high resolution image

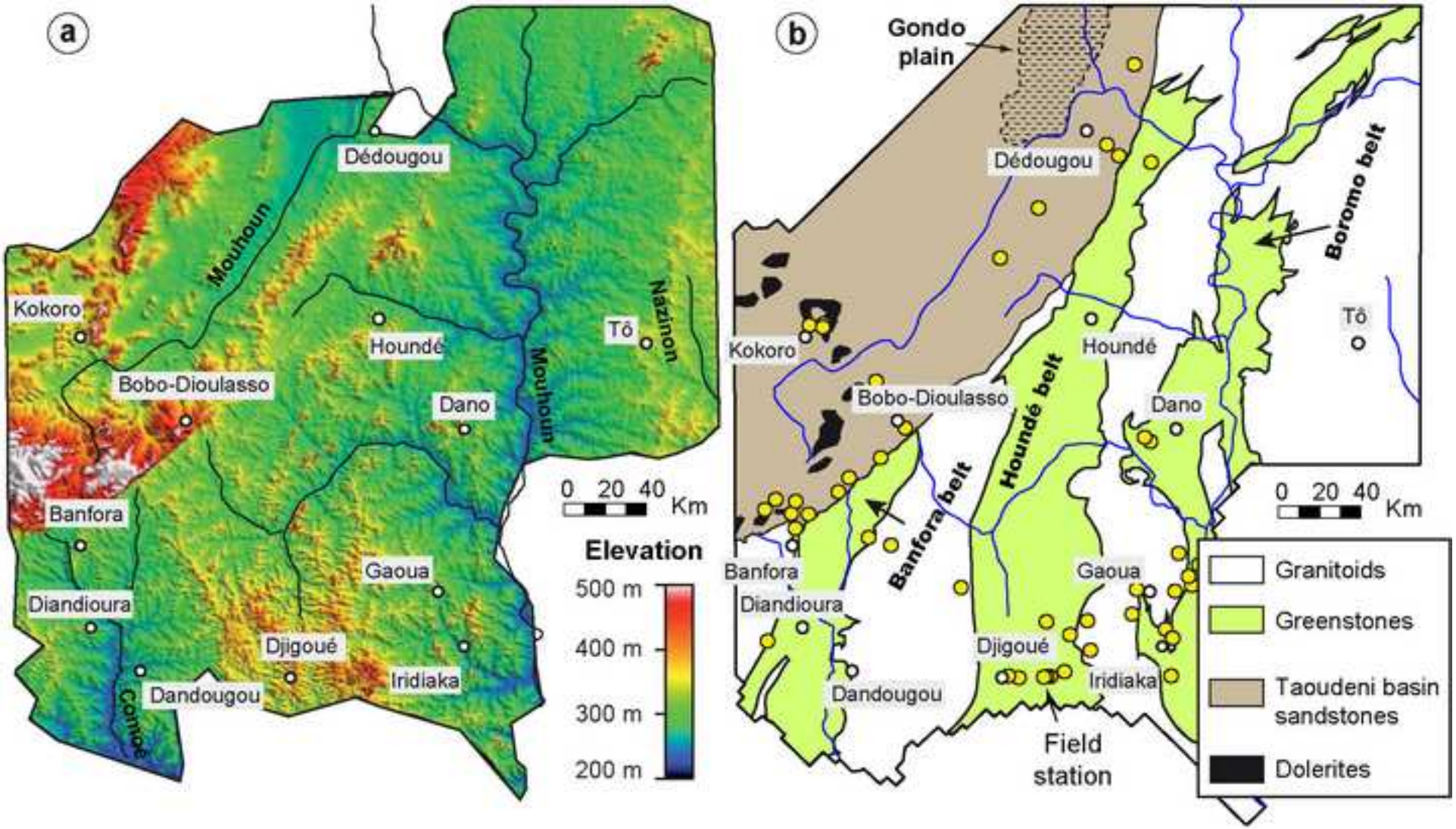

Figure 4

Click here to download high resolution image

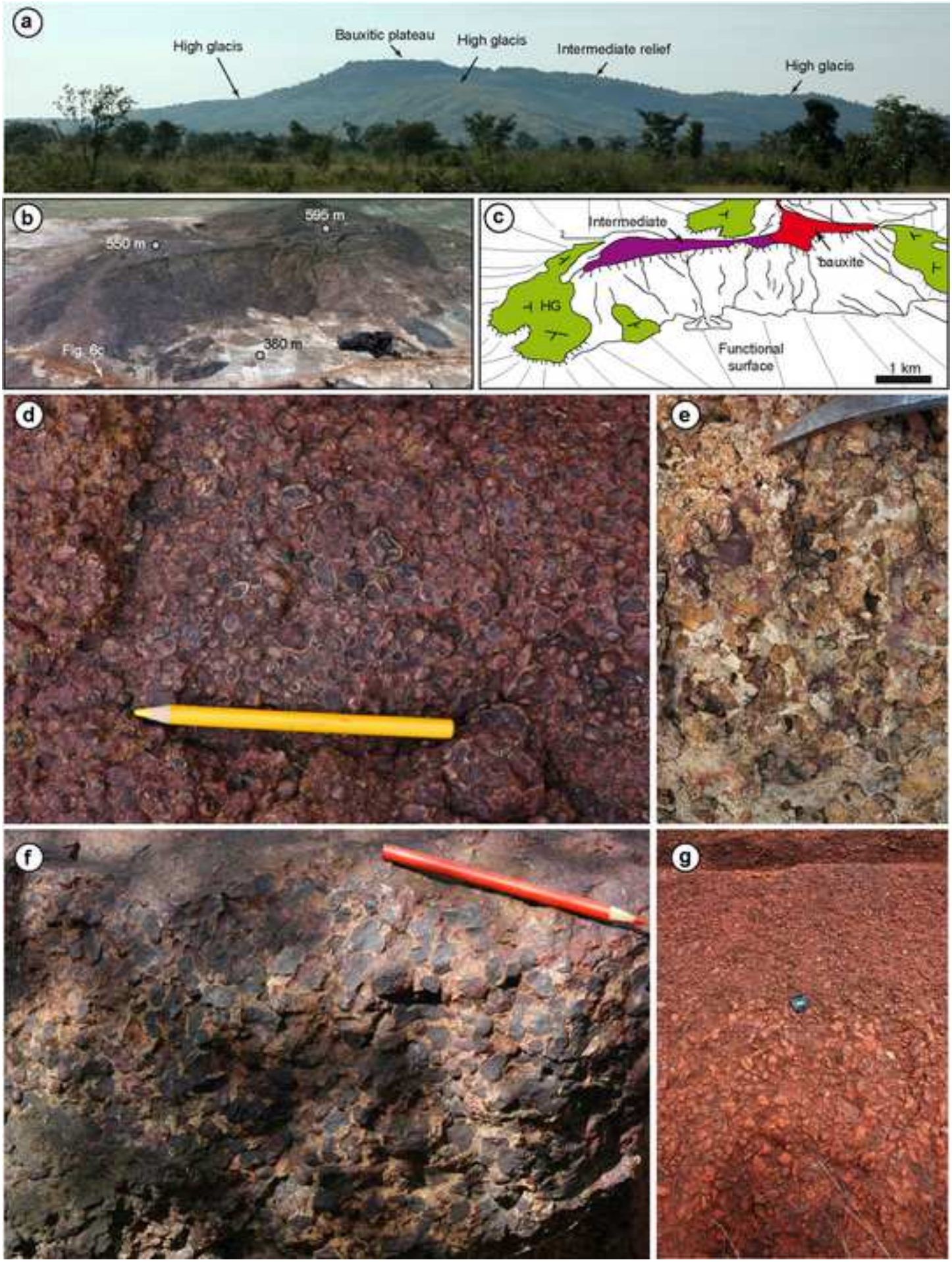

Figure 5

Click here to download high resolution image

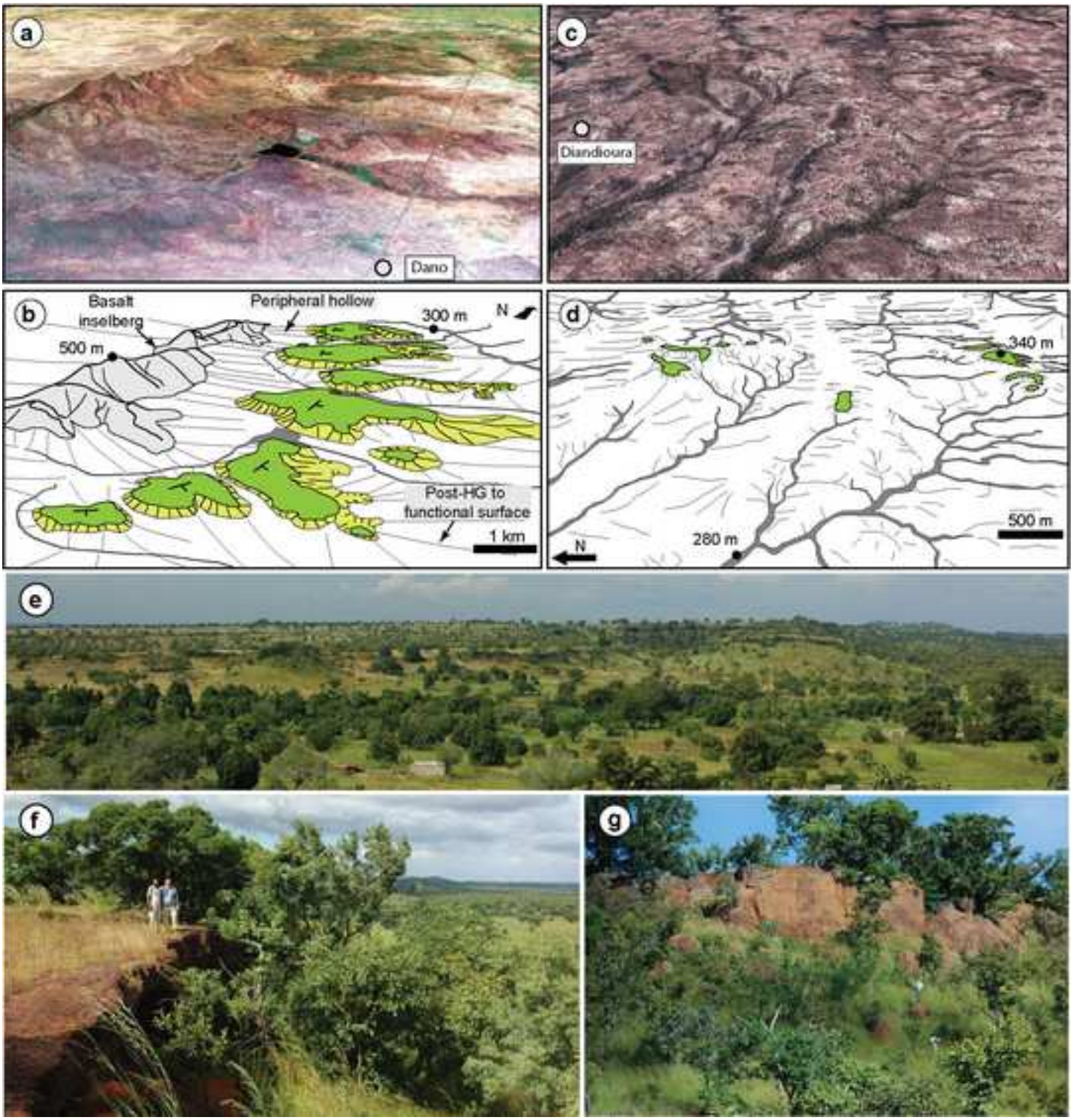

Figure 6

Click here to download high resolution image

Figure 7

Click here to download high resolution image

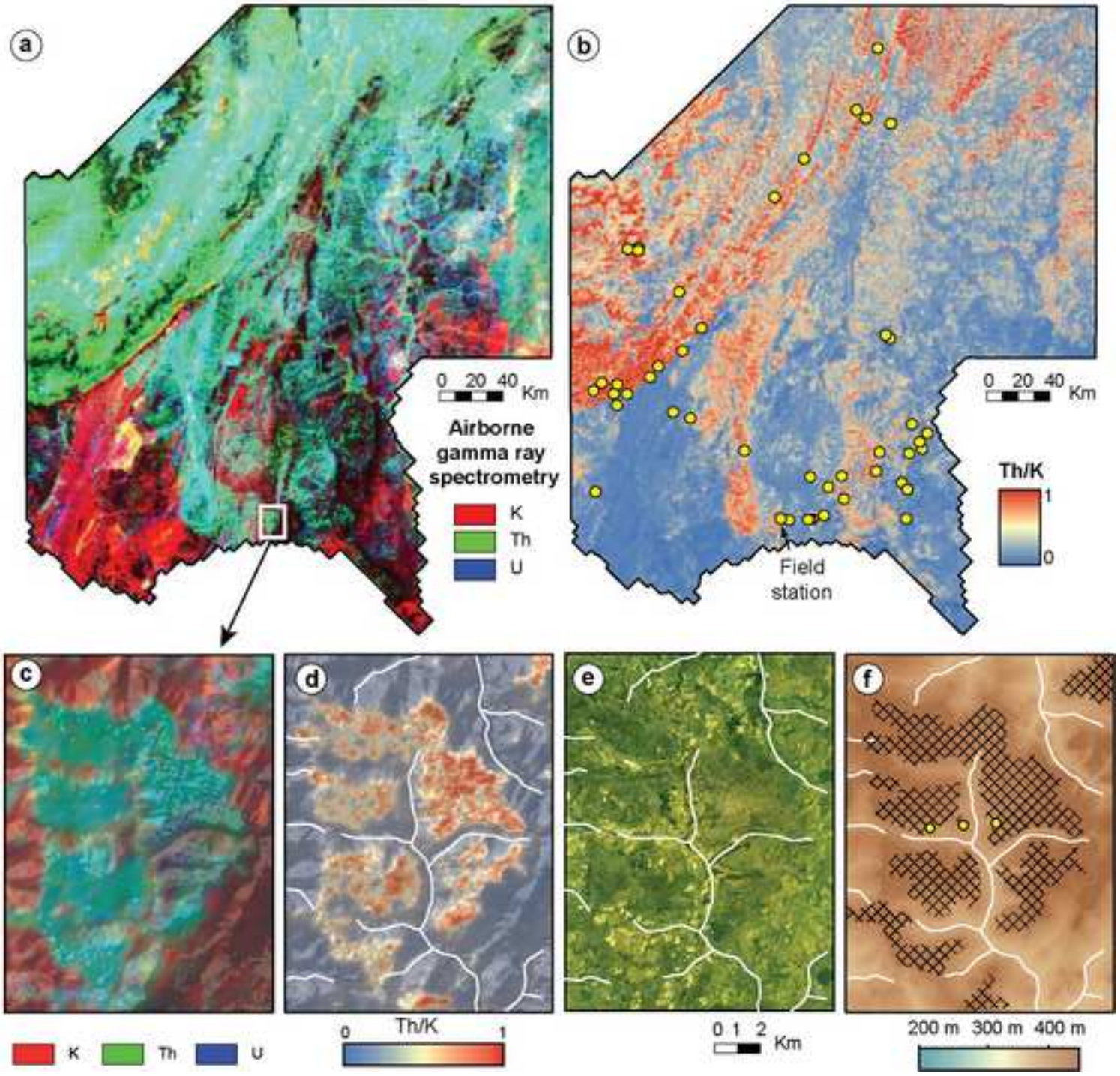

Figure 8

Click here to download high resolution image

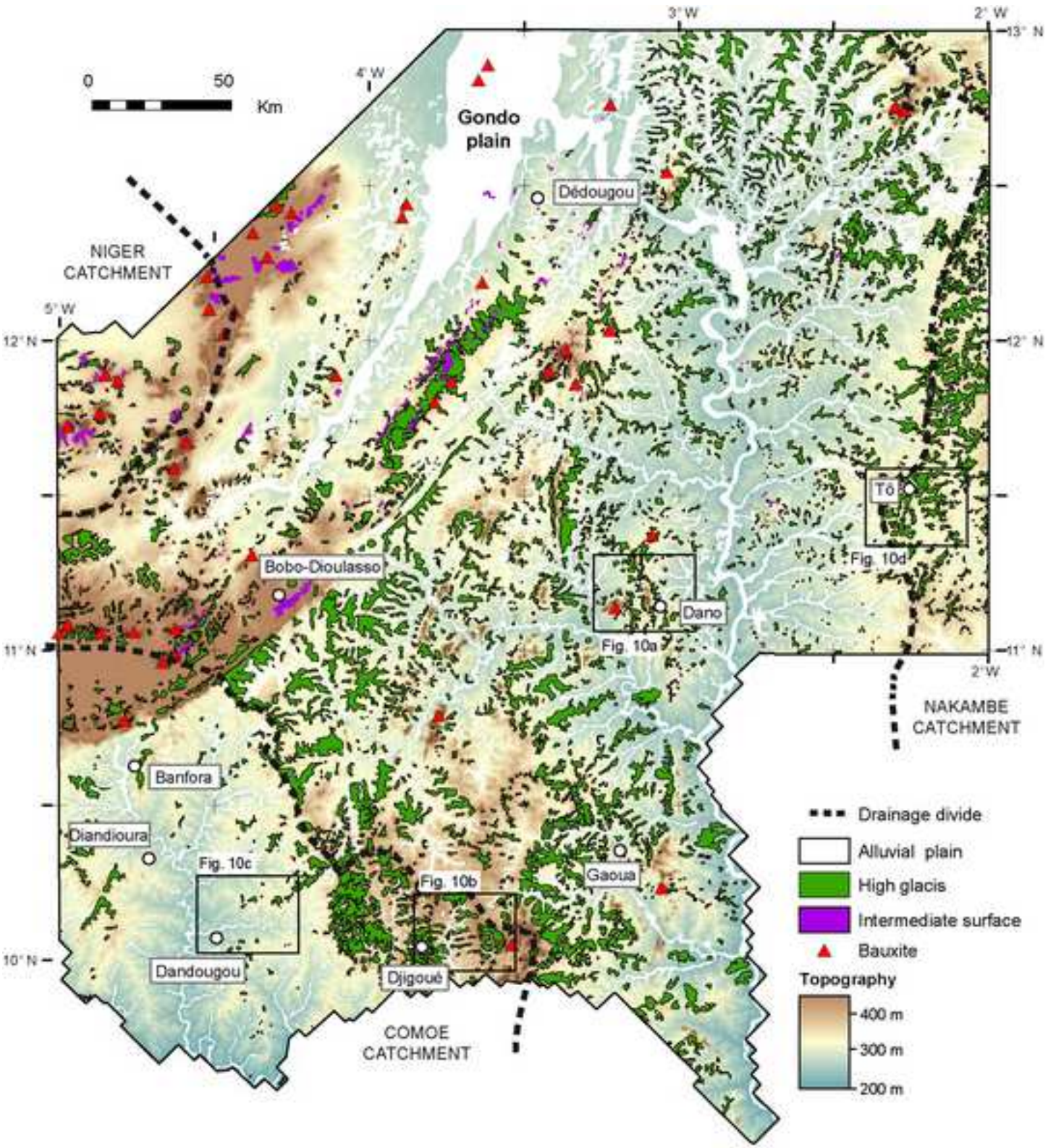

Figure 9

Click here to download high resolution image

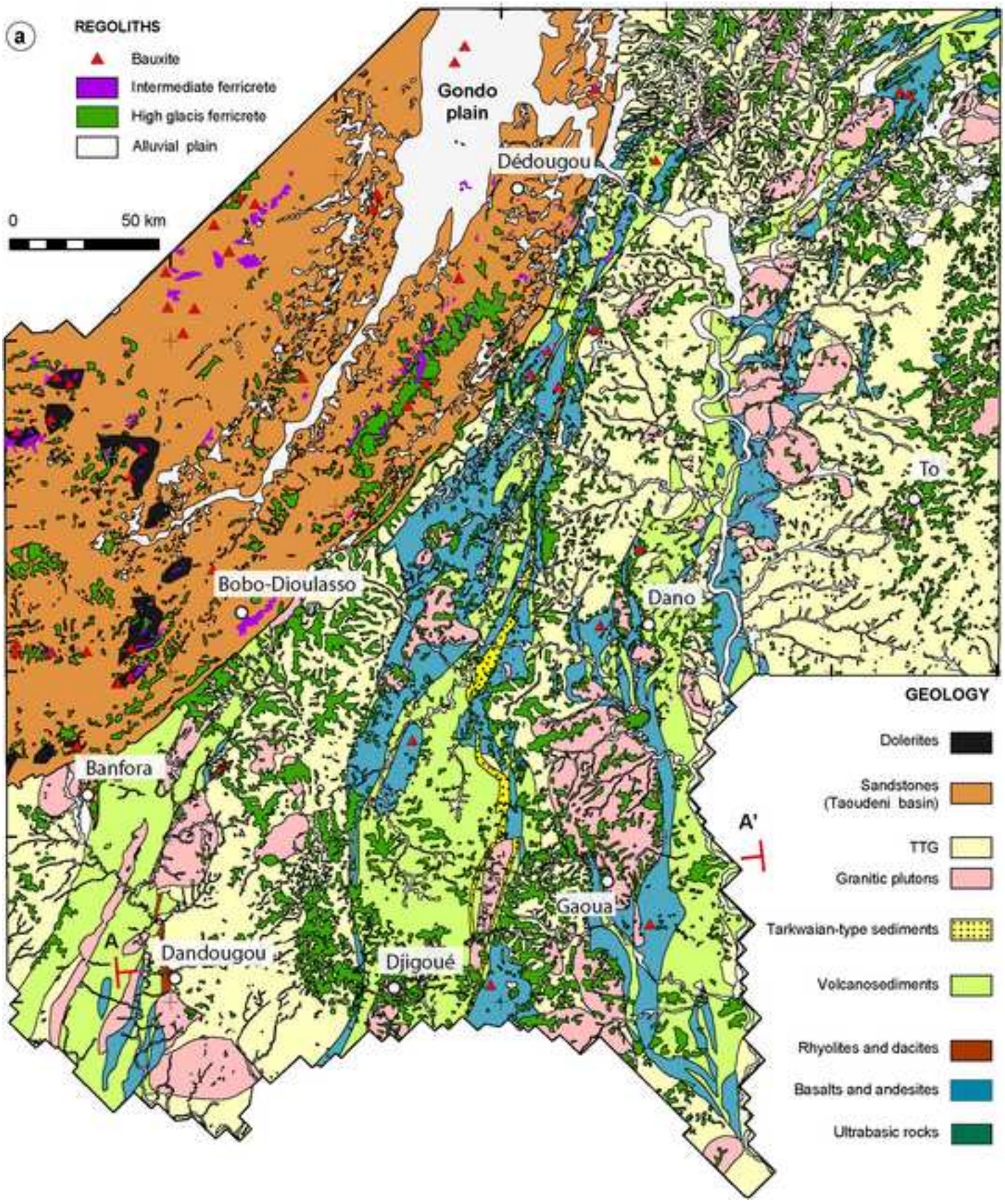

Figure 9bis

Click here to download high resolution image

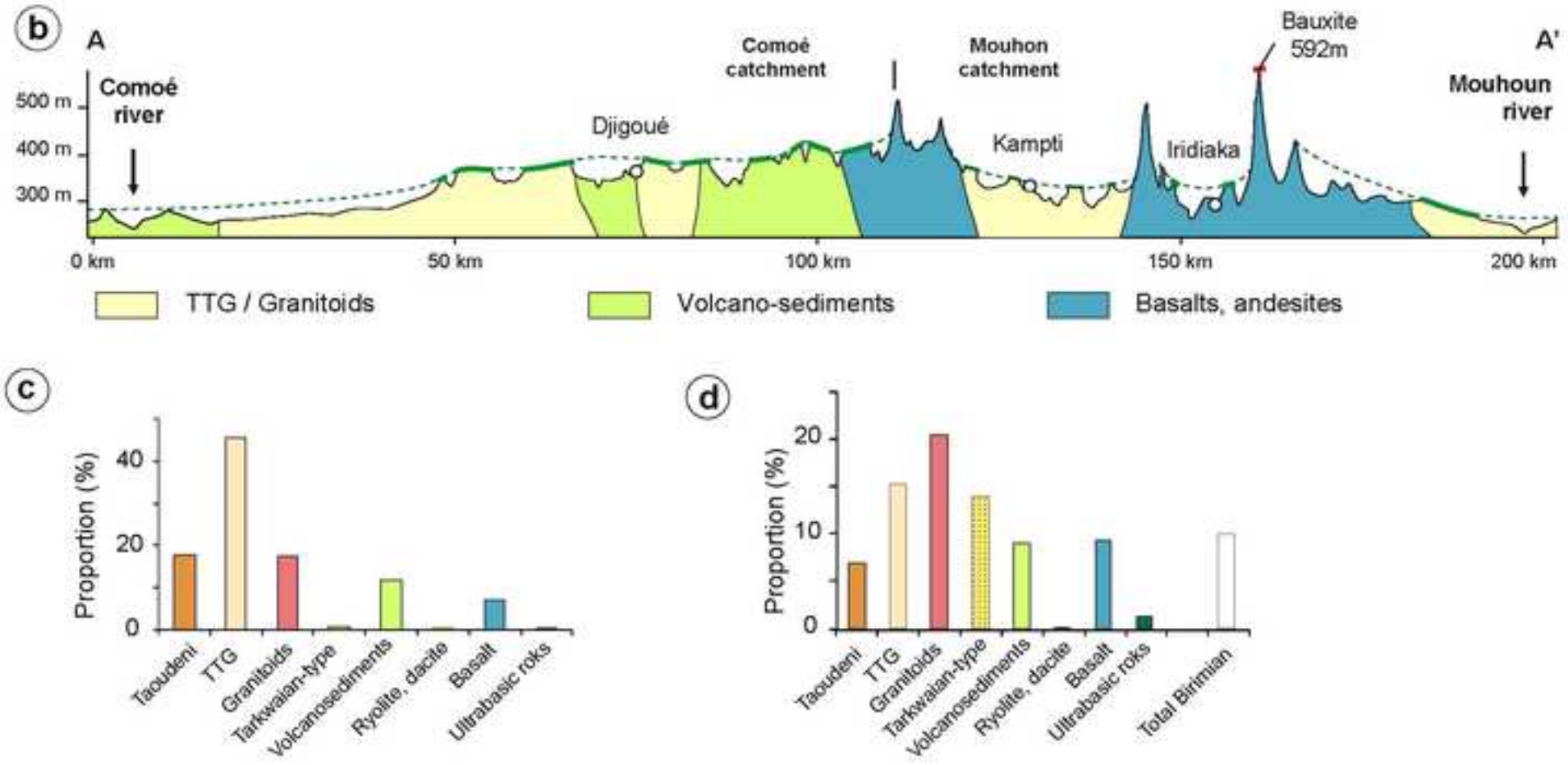

Figure 10

Click here to download high resolution image

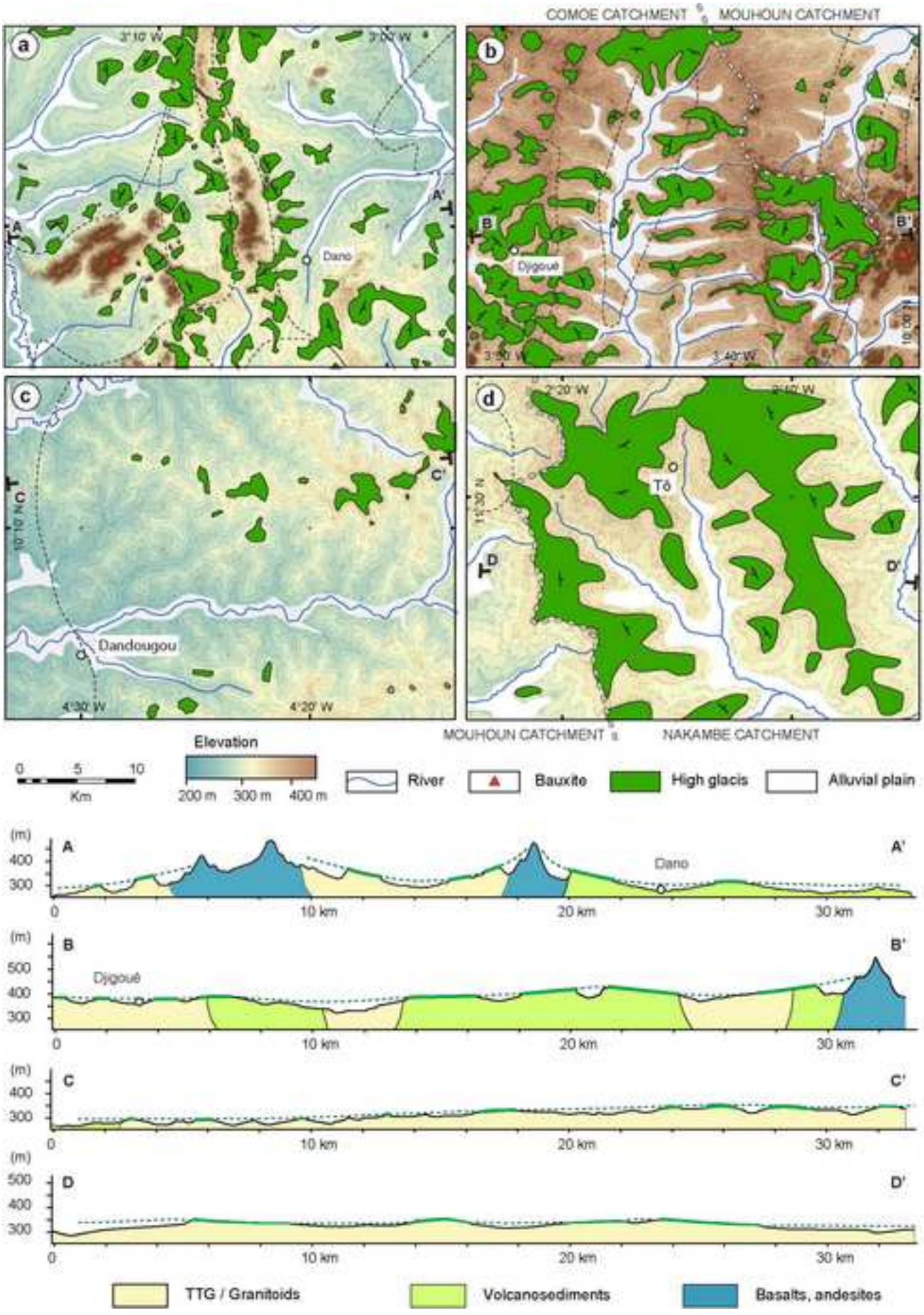

Figure 11

Click here to download high resolution image

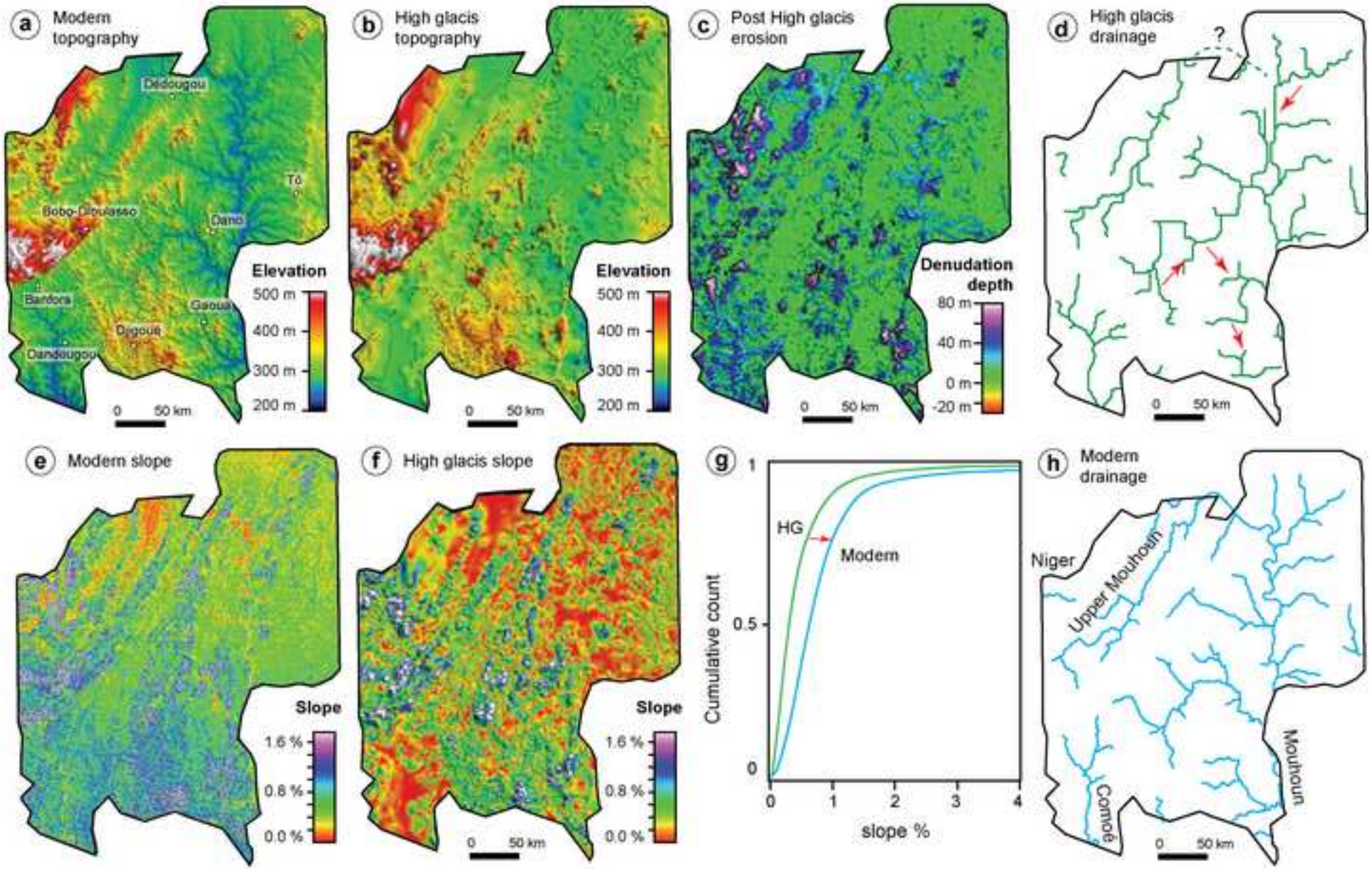

Figure 12

Click here to download high resolution image